

Lidar: Exploiting the Versatility of a Measurement Principle in Photogrammetry

Norbert Pfeifer, Gottfried Mandlbauer, Philipp Glira, Andreas Roncat, Werner Mücke, Vienna
András Zlinszky, Tihany, Hungary

ABSTRACT

In this article the principle of laser scanning is recapitulated starting from the LiDAR equation and the measurement possibilities, especially beyond the range measurement, are explained. This includes the radiometric measurement, bathymetric LiDAR, waveform capturing, new possibilities from UAV platforms, and single photon counting detection. It is demonstrated how these measurements can be used to derive land cover, models of topography, and to detect objects.

1. INTRODUCTION

Photogrammetry is often understood as a 3D reconstruction method of our environment based on the measurement of angles, directions, or rays, expressed through the collinearity equations. A first use of lasers for distance measurement in photogrammetry was thus a supporting tool for automating aerial triangulation (e.g. Kilian and Fritsch, 1993, Ackermann, Lindenberger, and Schade, 1992). Coupling satellite navigation by GPS and laser profile measurements provided direct georeferencing of aerial images, on the one hand, and parallax estimation, on the other hand. Alternatively, scanning the laser across the flight direction was understood as a technique for area-wise measurement over coasts and wadden sea (Ackermann, 1992), an area demanding for extracting homologous points and image matching due to the low texture of images acquired over these surfaces.

Airborne laser scanning as a method to capture 3D data of our environment was additionally strongly pushed by neighboring disciplines, especially hydrology (and hydraulic engineering), forestry, and geography. In forestry the ability to see into the forest was appealing, thus sensing a vertical profile from canopy to ground. It also gave the possibility to detect small forest openings at ground level. In geomorphology the high resolution of one point on 4 m² was appealing, because it allowed obtaining information on 3D shapes of unprecedented accuracy, thus enabling a better understanding of the processes forming the landscape. Likewise, floodplain modeling for hydrodynamic numerical simulation of flood events required detailed elevation information.

In photogrammetry airborne laser scanning research was first concentrating on terrain modeling, especially at forested sites (Kraus and Pfeifer, 1998), see also references in Sithole and Vosselman (2004), a comparison of terrain extraction methods based on an OEEPE dataset, and Korzeniowska et al. (2014). Calibration and accuracy were not in focus first, because terrain elevation measurement in forests became for the first time feasible through ALS (Airborne Laser Scanning). Thus, improving precision was not initially in the focus. Only later calibration became a topic of wider interest, leading to strip adjustment (Fritsch et al., 1994). Building extraction and building modeling from ALS point clouds was a research topic as well, which has long been in the interest of photogrammetry.

Terrestrial laser scanning developed in a certain way independent from airborne laser scanning. One reason may be that the manufacturers of scanners were different, another might have been that close range vs. topographic approaches were putting different requirements on processing and analysis of

data. The photogrammetric application of TLS was in established fields, thus concentrating on cultural heritage, on the one hand, and engineering applications, on the other hand.

However, the LiDAR principle allows more than “performing photogrammetry” with a different measurement device. It allows new types of observations and builds a bridge to remote sensing. It gives a possibility to engage with neighboring disciplines by exploiting and providing the knowledge on the measurement principle. These ideas will be explored in the following sections.

2. LIDAR PRINCIPLE

The approach taken here is to start rather from the LiDAR equation (see later Eqs. 2, 3) than from the polar measurement principle (Eq. 1).

$$\begin{pmatrix} X \\ Y \\ Z \end{pmatrix} = \begin{pmatrix} X_0 \\ Y_0 \\ Z_0 \end{pmatrix} + \mathbf{R}(\omega, \varphi, \kappa) \mathbf{R}(\alpha, \beta) \begin{pmatrix} r \\ 0 \\ 0 \end{pmatrix} \quad (1)$$

The exterior orientation of the platform (X_0, \dots, κ) may be dynamic or indexed for static setups. The observations are the angles α and β and the range r . Adding the range r is – in some way – similar to transforming a theodolite to a tacheometer by adding the laser range finder. As an addition, the laser range finder may provide two ranges in case of an ambiguous return signal. Considering the area coverage of photogrammetry, induced by the image area in the focal plane, laser scanning would thus be a “polar photogrammetry”. However, when starting from the LiDAR equation, the physical aspects are dominating, giving rise to the questions of the wavelength used, the interaction of EM radiation with the terrain surfaces (the scattering mechanisms), and the power received. This bears a similarity to the radiometric calibration of aerial cameras (Markelin, Honkavaara et al., 2008).

2.1. LiDAR equation

The LiDAR equation is similar to the RADAR (RADiowave Detection And Ranging) equation. It relates the power of the emitted light to the power received at the detector (Jelalian, 1992). The time lapse between emission of the signal and receiving its echo provides the ranging capability. However, as Measures (1992) once put it, additional observations become possible, thus LiDAR (LIght Detection And Ranging) should rather stand for Light Identification, Detection, Analysis and Ranging.

In the static form, the LiDAR equation relates the emitted power P_E to the detected power P_D (Jelalian, 1992, Wagner et al. 2003, Wagner et al. 2006).

$$P_D = P_E \cdot \frac{1}{(\gamma_E R)^2 \pi / 4} \cdot \sigma \cdot \frac{(D_D)^2 \pi / 4}{4R^2 \pi} \cdot \eta_{ATM} + P_B \quad (2)$$

The laser signal is emitted with the opening angle γ_E , travels through the atmosphere (Factor η_{ATM}), is scattered at an object (σ) in distance R , travels back through the atmosphere and is detected (lens/telescope diameter/aperture D_D). The background power P_B adds to the detected signal. The first fraction in the above formula has in the nominator the illuminated area at distance R , and multiplied with P_E the power density at a target, the second fraction is the ratio of the detector area to the area of the omnidirectional backscatter at distance R , a sphere. In this form all target properties are found in the target cross section σ . The cross section can be understood as area crossing the beam direction. It's unit is thus m^2 , representing an effective area contributing to the backscatter.

The above equation is already a specialized form of the LiDAR equation. It assumes a coaxial system, in which the illuminated area is always in the field of view of the detector (Riegl et al., 1974, Pfeifer et al., 2008). Otherwise, a geometric efficiency factor, $\eta_{GEOM}(R)$, becomes a multiplicative term to be considered additionally. Furthermore, it only applies in the far field, in which a linear widening of the signal holds. It also assumes single scattering, thus multiple scattering of a photon before detection is neglected. Additionally, the backscattered signals caused by different particles (or surfaces) are independent of each other, thus no phase relation between the individual returns exists. Polarization is not considered.

The power terms P_x ($x = D, E, B$) may also be replaced with the number of photons N_x , keeping however in mind, that N_D is the expected number of photons. The power terms are also functions of the wavelength λ . In “photogrammetric laser scanning” this is further restricted to elastic scattering, i.e. no change of wavelength (or frequency shift) due to scattering. Inelastic scattering is exploited, e.g., to detect water surfaces in bathymetric lidar (Guenther et al., 2000). A frequency shift in the return signal may also be caused by the Doppler effects of moving targets. The latter is exploited in wind lidar (Weitkamp, 2005).

2.2. Echoes, cross section, waveform, and radiometric measurement

The term σ is the target cross section and contains the target properties. If only the range to the target shall be determined, no further consideration is necessary. Also in this case, multiple echoes of topographic objects may be generated from one emitted pulse, if the first object along the laser beam does not fill the entire footprint, i.e. the illuminated area $((\gamma_E R)^2 \pi/4)$. Linear targets, as e.g. wires, only have a scattering area proportional to R , whereas single targets, e.g. a “single leaf”, have an area smaller than the footprint, independent of R (Jelalian, 1992). Extended targets have an area proportional to R^2 , and always cause only a single echo.

If, however, other properties than the range are additionally of interest (Wagner et al., 2003), the cross section σ is either split into the product of area A , reflectivity ρ , and scattering direction characteristics (homogeneous scattering into the solid angle Ω), $\sigma = A \cdot \rho \cdot 4\pi/\Omega$, or its value along the range direction is analyzed, leading to the differential cross section $\sigma(R)$. Both approaches need a formulation, in which the signal power is described as a function of time. With some simplifications and neglect of terms for the sake of clarity, and considering only one target, σ_i , at the representative range $R_{m,i}$, this leads to the dynamic LiDAR equation.

$$P_{D,i}(t) = \frac{D_D^2}{\gamma_E^2 R^4 4\pi} \int_{R_{m,i}-\delta}^{R_{m,i}+\delta} P_E \left(t - \frac{2R}{c} \right) \sigma_i(R) dR ; \quad \sigma_i = \int_{R_{m,i}-\delta}^{R_{m,i}+\delta} \sigma_i(R) dR \quad (3)$$

The integral is the convolution of the emitted signal with the differential cross section of the target, 2δ is the extent of the target in the range direction, and c is the speed of light (group velocity). Multiple echoes are superimposed onto each other and may overlap in $P_D(t)$, with $P_D(t) = \sum_i P_{D,i}(t)$. In waveform LiDAR $P_D(t)$ and $P_E(t)$ are sampled in fractions of the pulse duration. As the pulse duration for commercial topographic lidar systems is in the order of 2ns to 10ns, the sampling is correspondingly in the order of 0.5ns to 2ns. Without going further into technical details, this allows

- to determine the amplitude and width of detected echoes by analysing the sampled $P_D(t)$,
- to perform a deconvolution of $P_D(t)$ and $P_E(t)$ to obtain $\sigma(R)$, and in consequence
- to obtain σ from $\sigma(R)$.

With the additional assumption of Lambertian targets, i.e., diffuse scattering, and the known footprint area of an extended target, the diffuse reflectivity of a surface can be inferred from Eq. (4).

$$\sigma = \frac{(\gamma_{ER})^2 \pi}{4} \cdot \rho_{\text{diff}} \cdot \cos \alpha \cdot \frac{4\pi}{\pi}; \quad \rho_{\text{diff}} = \frac{\sigma}{(\gamma_{ER})^2 \pi \cos \alpha} \quad (4)$$

Here α is the incident angle, i.e. the angle between the surface normal and the direction of the LiDAR signal. If surfaces are sampled by scanning LiDAR, then the 3D position of the points can be used to estimate a surface and thus also α .

2.3. Wavelength

As written in Sec. 2.1 and 2.2 the reflectance of an object has an impact on the power of the detected echo and the LiDAR equation needs to be understood as a function of wavelength. Thus, the choice of wavelength for a topographic laser scanning depends not only on the transmittance through the atmosphere, but also on the objects to be studied. For snow, e.g., the choice of the commonly available wavelengths (e.g.) 1.064 μm and 1.550 μm make a notable difference (see Fig. 1). The figure demonstrates also, that if the object investigated is known, then some of its parameters may potentially be detected from the reflectance, provided a suitable wavelength is chosen. However, using the example of snow, its grain size is not the only parameter of influence but also snow impurities have an influence on the reflectance (Kuhn, 1985, Aoki et al., 2003).

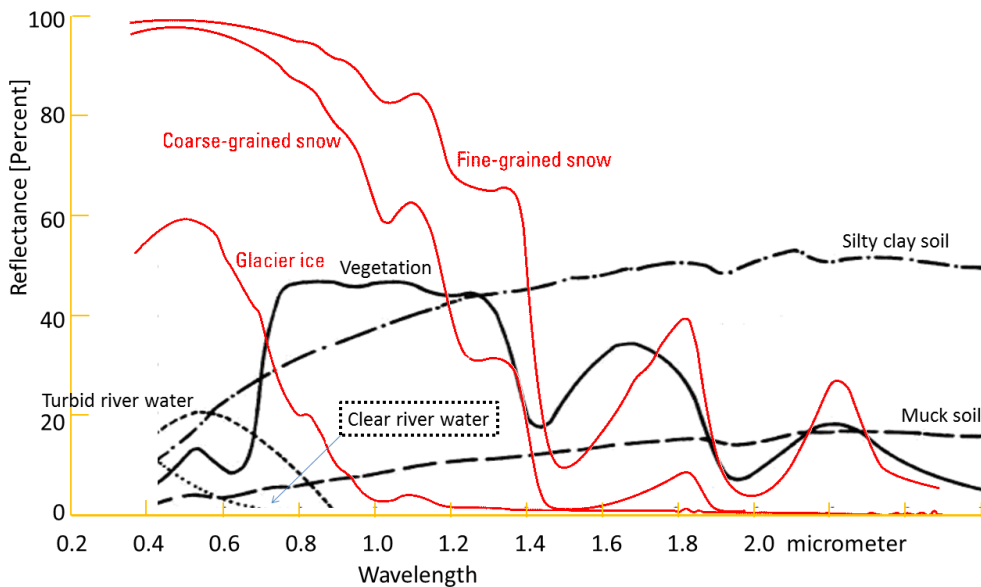


Figure 1: Reflectance curves for water, vegetation, and soil (Swain and Davis, 1979, www.usgs.gov).

Fig. 1 shows only one curve for vegetation. The health state, on the one hand, but also species cause deviations from this reflectance curve. Thus, multiple wavelength lidars are being developed for studying vegetation (Collin et al., 2010, Douglas et al., 2014). The low reflectance from clear water leads to measurement drop outs at longer wavelengths. At short wavelengths, especially in the visible green light, the light penetrates also the water column. Scattering and absorption are much stronger in the water than in air, thus the visibility is reduced to a few meters, depending on the power of the emitted signal, the turbidity of the water body, and the bottom reflectance. Bathymetric LiDAR, typically at 532nm, is a technology for measuring the bottom of rivers and sea, for a restricted depth zone.

2.4. Single photon counting

The detection of the backscattered signal in topographic LiDAR may be performed with APD (avalanche photo diodes), which convert the incoming power to an electric current, which may then be analyzed electronically (discrete return systems) or digitized (waveform recording).

APDs can also be operated to detect single photons (SPAD, Single Photon Avalanche Diode), which leads to single photon counting systems (Zappa et al., 2007), however SPC detectors can also be built with other means. The time of such a single photon detection event can be determined, leading to a range measurement. The probability that a photon is detected is proportional to the number of photons arriving at the detector. However, in this mode, the photo diode exhibits a dead time, which means that a certain time is required before a new photon can be detected. Also background photons, not originating from the measurement process, may be detected.

In time correlated single photon counting (TCSPC, Becker (2005)) short pulses are emitted at a high repetition rate in a static setting. From each pulse one backscattered photon is detected. The differences between the time of the detection event and the corresponding pulse emission are sorted in a histogram, which is further analyzed (e.g. mode detection, cross correlation with a reference pulse shape, or statistically more advanced estimation (Hernández-Marín et al., 2007)). To mitigate the effect of the dead time of a single detector, detector arrays may be used, thus enabling a range measurement from one pulse.

Single photon counting (SPC) is a possibility to detect very weak signals, e.g. for LiDARs on satellite platforms observing the Earth (Degnan, 2001).

3. EXAMPLES

The versatility of the LiDAR measurement principle was described above from a theoretical point of view. In this section it shall be demonstrated by examples. The sources of these examples are mentioned, but of course similar work can be found at a number of institutions.

3.1. Precise ranging

An advantage of LiDAR is the direct 3D measurement. Cameras have the advantage of higher resolution, physically bounded because of the aperture diameter (beam divergence vs. diffraction blur), and the resolution of image matching surface models may be close to that of the images. However, points provided by (pulsed) laser scanning systems are in that sense more reliable, that they originate in almost all cases from reflecting surfaces. The continuity assumption of image matching may lead to points on a virtual ramp from one surface level to another.

Measurement precision of LiDAR ranging is in the domain of a few mm for terrestrial laser scanners, e.g. up to 100m, and in the domain of cm for airborne laser scanning. Thus, the dominating error sources originate in georeferencing. Using the overlapping areas of strips the lidar system can be calibrated on the job while the georeferencing can be improved. Algorithms have matured and the trajectory can be improved by time-dependent functions (e.g. splines), provided overlap is sufficiently strong (Glira et al., 2015ab). In that sense, strip adjustment has reached the same versatility as bundle block adjustment of images.

As illustrated in Fig. 2, airborne laser scanning provides a precision of a few centimeters. Of course, rough areas are subsampled and elevation changes are only significant over larger areas. Using multi-epochal strip adjustment, introducing geologically stable areas as tie-area between two epochs, allows detecting small height changes (stable areas show changes below 2cm) and relate them to changes in the perma-frost and other geomorphological processes (see, e.g., Heckmann et al., 2015).

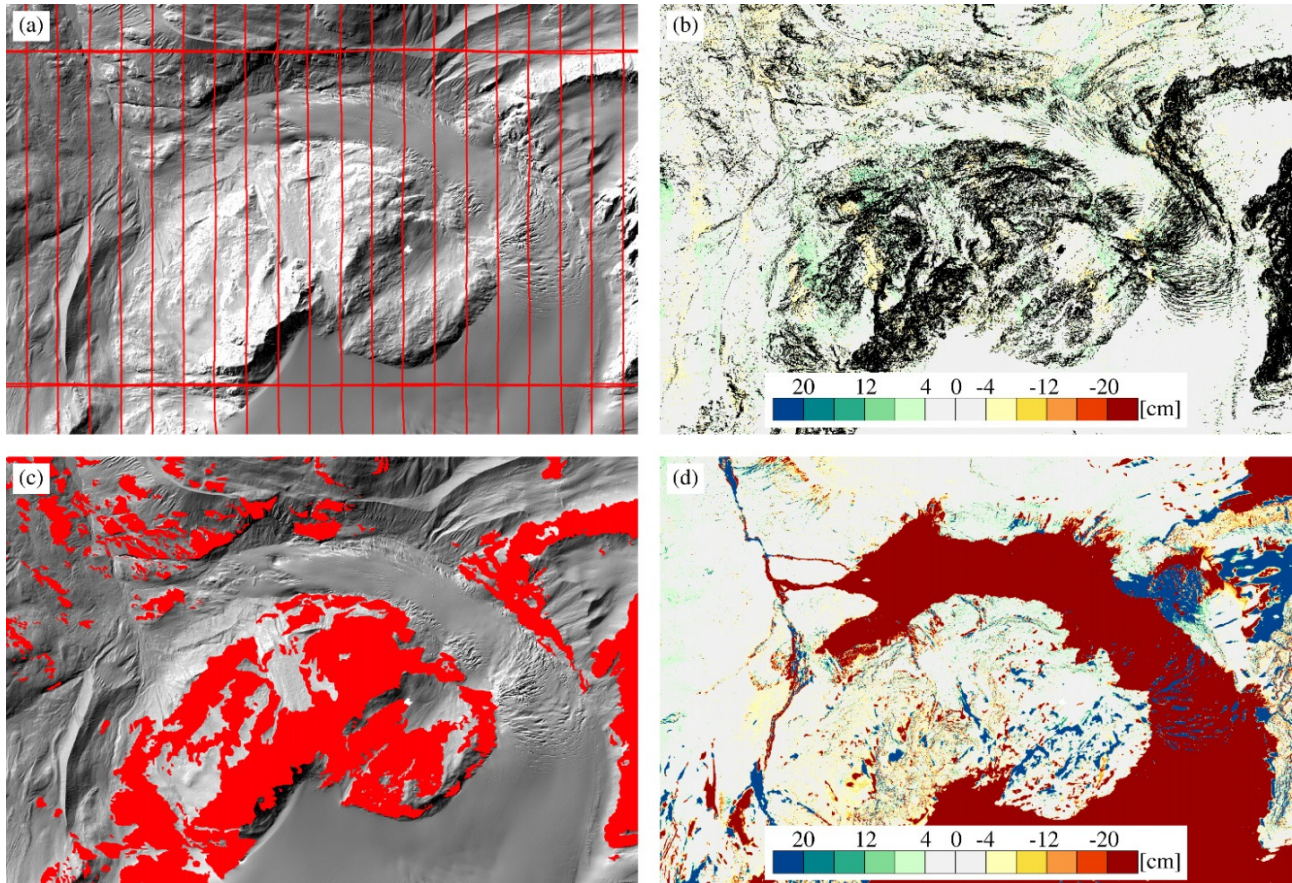


Figure 2: (a) Shaded relief map with overlaid flight lines of a glacier in the Alps. (b) Residual strip height differences after strip adjustment within one flight mission (masked to use only smooth areas). (c) Stable bedrock areas (red) mapped by geologists. For multi-epochal strip adjustments, correspondences are only established within these areas. (d) Height differences between two epochs (from July to September).

3.2. Waveform, Echo Width, and Reflectance

Detecting the ground below the canopy is a consequence of both, the multi-target capability of pulsed lasers due to short pulses leading to temporally distinct echoes, and the monostatic setup of the LiDAR. The latter means that the gap in the foliage used to illuminate the ground with the laser is the same gap used by the echo to reach the detector.

Still, this means that not all last echoes over forested areas are from the ground. It is especially difficult to distinguish between echoes from low vegetation above the forest ground and the “real” forest ground. However, vegetation typically has a larger height distribution within the footprint area than ground, thus a wider differential cross section $\sigma_i(R)$. This can be used to increase the reliability of ground extraction and in consequence also to detect solid objects on the ground.

As illustrated in Fig. 3, the waveform information supports extraction of downed stems by an improved separation of low vegetation and forest ground (Mücke et al., 2013). Waveform information is also beneficial for classifying vegetation as such, also within grass lands. Fig. 4 shows a classification of a protected grassland habitat based on machine learning from field reference data. The data was acquired at two phenological states (July 2011 and March 2012), with a density of 12.8 points/m². The features used were measures of point distribution in various neighborhood size, calibrated reflectivity, and echo width (Zlinszky et al., 2014).

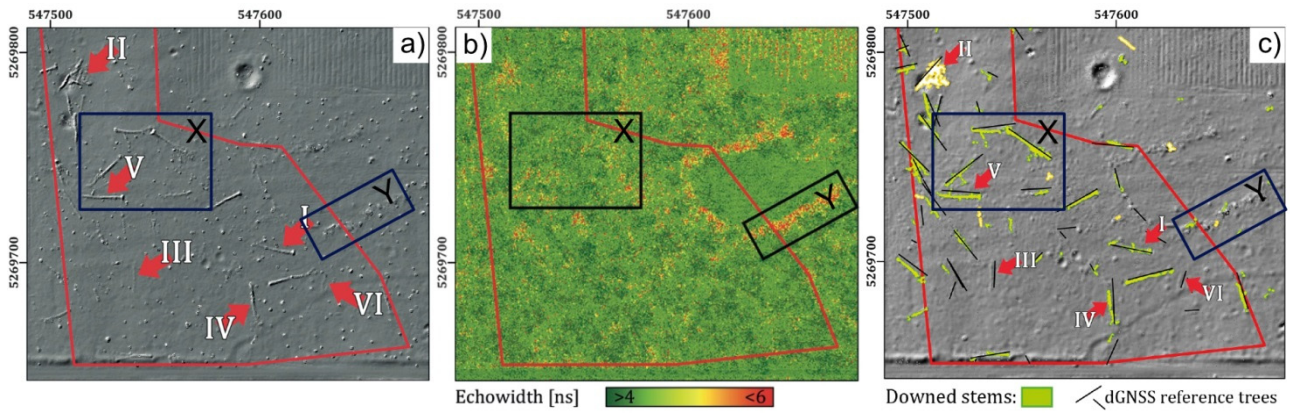


Figure 3: (a) Shaded relief map of forest ground, locations I – VI showing downed stem candidates; (b) echo width map, (c) detected downed stems, black lines indicate GNSS-measured stems for reference. The black rectangles X and Y indicate two areas of low (X, echo width <4 ns) and high (Y, echo width > 6ns) echo widths. While X represents true forest ground and downed stems as solid objects, Y results from shrub and herbaceous vegetation.

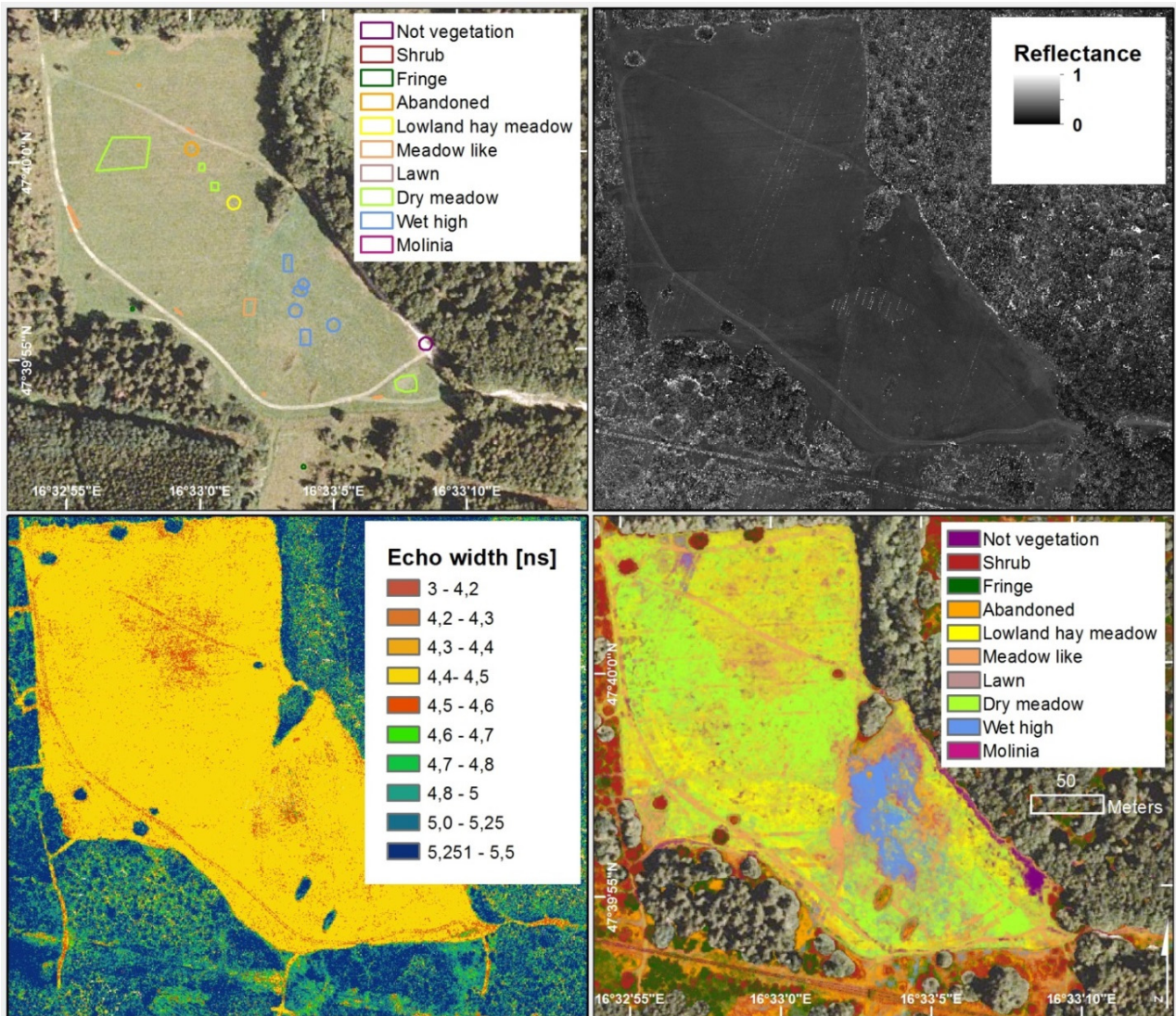


Figure 4: Ortho photo of grass land, calibrated reflectance, echo width, and classification based on lidar waveform data of two epochs.

Small footprint LiDAR is only one option for studying vegetation, including also urban vegetation (Rutzinger et al., 2008). Medium-sized and large footprint LiDAR provides information over larger areas and thus spatial aggregation (Lefsky et al., 2005), which can be selected to fit the size of the objects studied.

3.3. Wavelength

Classification of objects in our environment profits improves, if multiple, complementary measurements are available. Image matching can provide geometry and the images themselves provide color, or even calibrated reflectance (Markelin et al., 2008). Hyperspectral imaging can be argued to be “superior” because each pixel has a high number of measurements (Asner, 2013). As mentioned in Sec. 2.3 multiple wavelength systems are being developed (Vauhkonen, Kaasalainen et al., 2013, Puttonen et al., 2014), allowing, e.g., the determination of NDVI per detected echo. However, not only the reflection strength can be used. Höfle et al. (2009) showed that absorption can be used to detect water surfaces, and transmission (and reflection at other surfaces) is exploited in bathymetric LiDAR. From all visible and infrared wavelengths the green light is the one to propagates best into and in the water. This is exploited in bathymetric LiDAR. A green LASER pulse is emitted from the sensor, travels through the atmosphere, is refracted at the water air interface, travels through the water column (with stronger absorption and scattering), hits the river or ocean ground surface, and travels the same way back to the sensor. Over dry land reflections are caused by surfaces. However, the different reflection properties at green light (e.g. 532nm) in comparison to the standard topographic wavelengths (e.g. 1064nm and 1550nm) need to be considered (see Fig. 1).

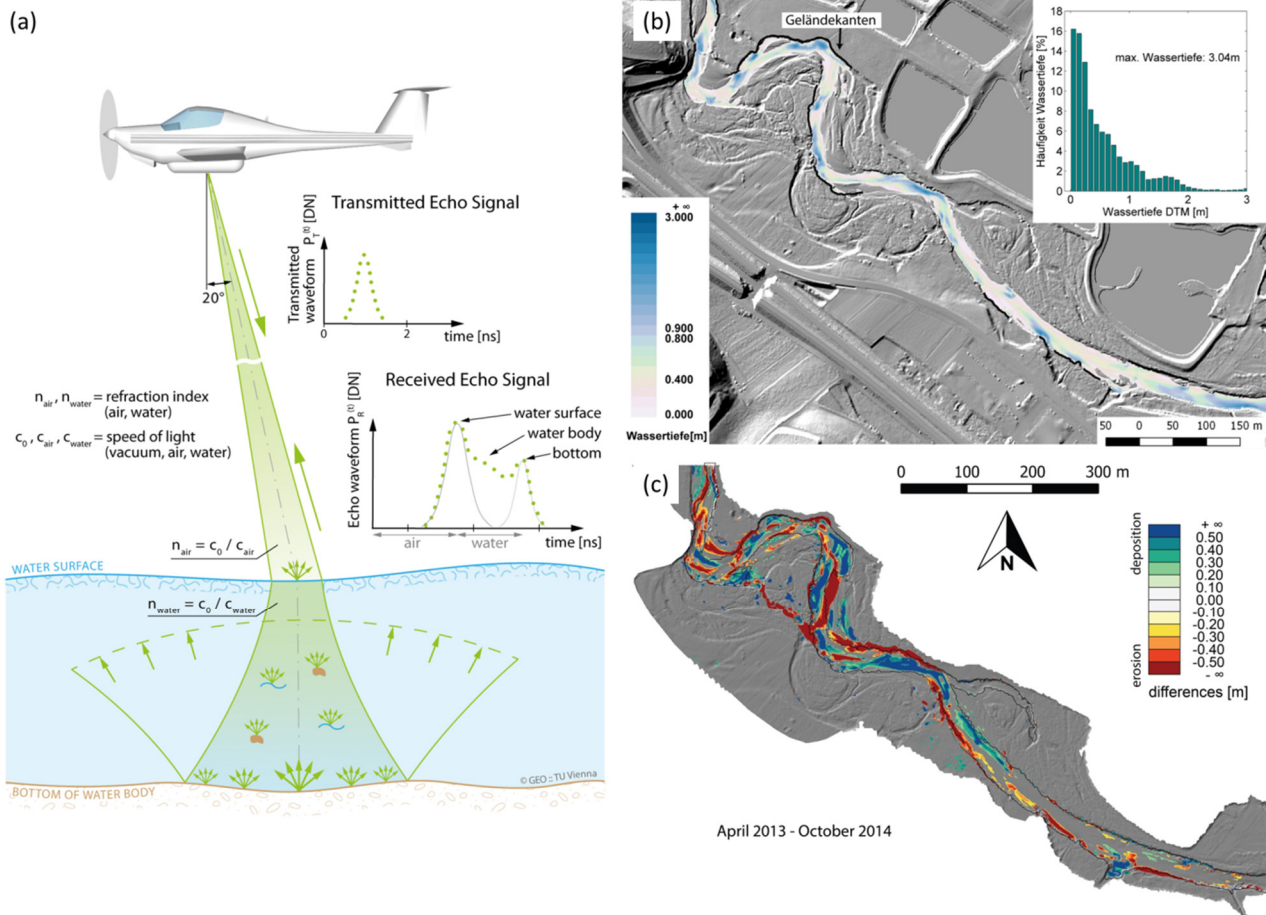


Figure 5: (a) Bathymetric LiDAR measurement principle, (b) shaded relief map and water depth, (c) deposition and erosion of material due to a 30-year flood in the main channel and temporary side channels during the flood.

As illustrated in Fig. 5, the river channel and the alluvial area can be acquired simultaneously with airborne laser scanning using a green LiDAR (Mandlbürger et al., 2015a). This requires automatic classification of echoes into dry ground, wet ground, water surface, and vegetation (and other objects). This is intertwined with modeling of the water surface which is required for refraction correction.

3.4. UAV LiDAR

LiDARs are active instruments, thus they need a power supply. The scanning mechanism requires additionally moving parts, adding to power consumption and weight. Thus, cameras are more frequently mounted on remotely piloted airborne systems (RPAS) or UAVs (unmanned aerial vehicles), see, e.g., Fritsch and Cramer (2013). However, low flying UAVs with a laser scanner can provide point clouds of higher resolution (Mandlbürger et al., 2015b, Pfennigbauer et al., 2014). Lower distances from sensor to target also leads to smaller footprints, but demands on georeferencing are growing as well.

A vision is to make engineering surveys of infrastructure lines (e.g. streets, maybe excluding tunnels for the time being) rather from airborne platforms than from terrestrial positions. Another application, demonstrated in Fig. 6, is to identify trees in the forests not by their canopy (Lindberg et al., 2014), but by their stem. This would allow modeling diameter at breast height (DBH) from the point cloud rather than inferring it from allometric relations between DBH and tree height. At this point also LiDAR mounted on quads for forest inventory is an interesting option (Kukko et al., 2012). While georeferencing may be more demanding, bringing the sensor even closer to the objects of study may be of interest.

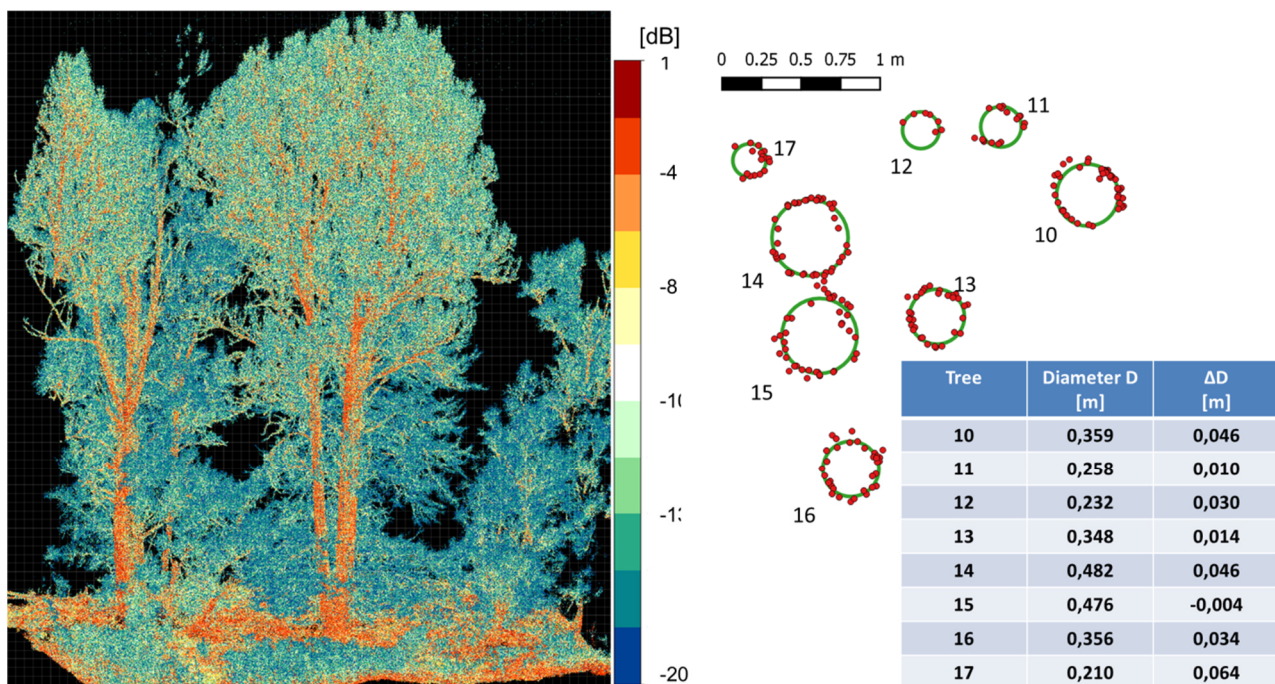


Figure 6: Left: UAV LiDAR point cloud of riparian forest colored by target reflectance. Right: The point cloud at 1.2 to 1.4 m above ground is shown (red dots), together with automatically detected and fitted circles (green). For each tree, the estimated diameter and the deviation from in-situ measurements are plotted.

3.5. Single photon counting

Single photon counting LiDARs are flown in airborne experiments, e.g. MABEL (Multiple Altimeter Beam Experimental Lidar, in preparation of NASA's ICESat 2 mission, see Brunt et al. (2011)), but not used for operative (satellite) missions yet. Single photon LiDAR data is a set of photon detection events. In that sense it has the same “format” as discrete return single echo laser scanning data. A photon detection event relates to a certain time, but has no additional parameters (like amplitude or echo width). It can be georeferenced knowing the exterior orientation of the sensor and the time lapse between emission and detection. Using array detectors, multiple photons are received, adding up to a certain numbers of events per time slice, which has a “format” similar to a waveform.

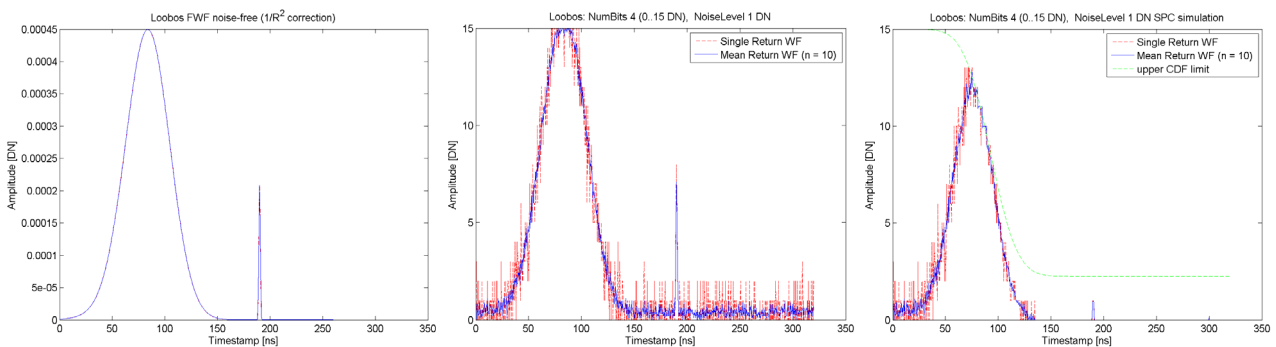


Figure 7: Left: simulated differential cross section of tree crown and ground; middle, red curve: detection events of an array SPC sensor without dead time, blue curve: average of 10 signals; right: detected signal using a dropping detection probability as typically given. Here, the photon detection efficiency is an inverted Gaussian CDF. Note the reduction in peak size of the ground return.

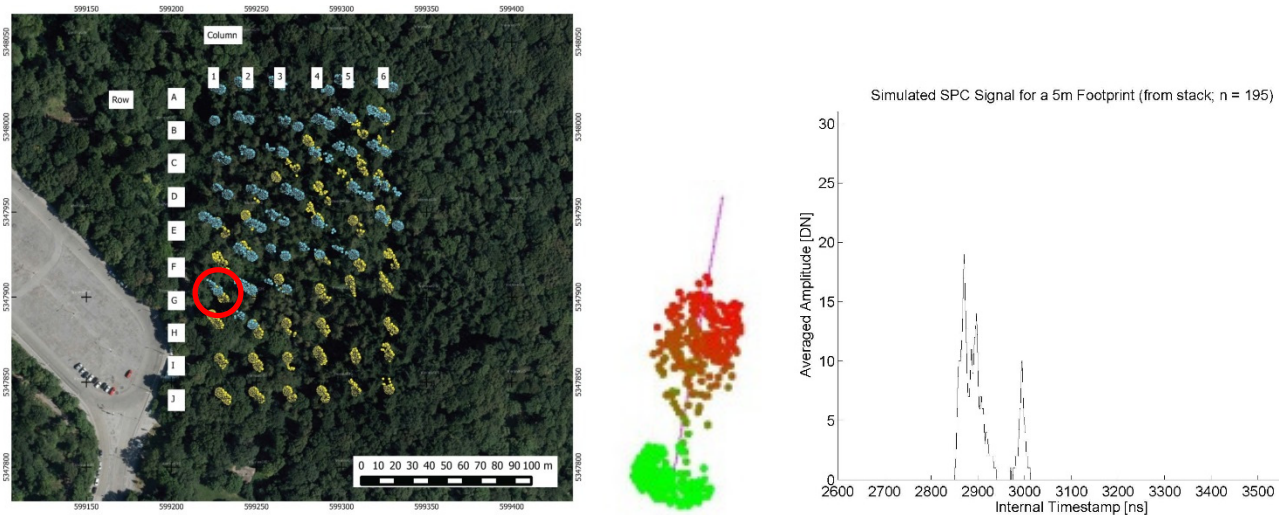


Figure 8: Left: ortho photo over a douglas fir plot, points selected in cylinders of 5m diameter along the shot direction of a waveform dataset, middle: selected points colored according to height, right: simulated SPC detector signal based on the waveform LiDAR data considering the drop in photon detection efficiency.

Figs. 7 and 8 show simulations. SPC data from airborne platforms was also used to estimate tree height (Awadallah et al., 2014), with differences to tree height estimated from standard LiDAR data in the order of a few decimeter.

4. CONCLUSIONS

In this article the versatility of the LiDAR measurement principle was demonstrated: choice of wavelength, multi-target capability, waveform, radiometric measurement, single photon counting. Further features not mentioned are polarization and footprint size. While starting from a more physically oriented description, the scanning pattern and area coverage introduces leads to concepts and models very similar to those derived from image-based photogrammetry. This includes strip-adjustment, classification, and effects or requirements related to the sensor carrying platform. This article introduced also a number of differences between measuring and modeling from photographic images and scanning LiDARs, while some were not mentioned: resolution, reliability, precision, physical quantities vs. relative measures (texture), penetration depth into vegetation canopy, etc. However, even more interesting is to exploit those differences to reach a more efficient and comprehensive description of our environment. This domain is largely unexplored.

5. ACKNOWLEDGEMENTS

The work presented in this article was derived during and with support of the following projects: Airborne Alpine Hydro Mapping—From Research to Practice (FFG COMET-K), ChangeHabitats2 (EU FP7 IAPP), PROSA (DFG/FWF), ALART (ESA). I am especially grateful to Philipp Glira, Werner Mücke, András Zlinszky, Gottfried Mandlbürger, and Andreas Roncat for their support to this article.

As a personal note I acknowledge the support of Dieter Fritsch to EuroSDR (former OEEPE). During his presidency and with his strong support much of the above mentioned research was pushed further by benchmarks and other projects. While also driven forward by others, this includes – amongst others – the radiometric calibration of aerial cameras (EuroSDR Report 62, 2013), exploitation of UAVs, single tree detection (EuroSDR Report 53, 2008), combination of LiDAR and photos (EuroSDR Report 59, 2011), and high density image matching (EuroSDR Reports 61, 2012 and 63, 2013), see also www.eurosd.net.

6. REFERENCES

- Ackermann, F. (1992). Laserabtastung zur Küsten- und Wattvermessung. *Zeitschrift für Vermessungswesen*, Heft 8/9, 5, pp. 498-507.
- Ackermann F., Lindenberger, J., Schade, H. (1992). Kinematische Positionsbestimmung mit GPS für die Laserprofilmessung. *Zeitschrift für Vermessungswesen*, Heft 1, 5, pp. 24-35.
- Aoki, T., Hachikubo, A., Hori, M. (2003). Effects of snow physical parameters on shortwave broadband albedos. *Journal of Geophysical Research*, 108(D19), doi:10.1029/2003JD003506.
- Asner, G. (2013). Biological Diversity Mapping Comes of Age. *Remote Sensing*, 5(1), pp. 374-376, doi:10.3390/rs5010374.
- Awadallah, Ghannam, Abbott, Ghanem, (2014). A Two-stage Algorithm for Extraction of Ground and Top of Canopy in Photon-counting Profiling-LiDAR Data in Preparation for The ICESat-2 Mission. IGARSS 2014.
- Becker, W. (2005). *Advanced Time-Correlated Single Photon Counting Techniques*. Springer.

- Brunt, Neumann, Markus, Cook, Hart, Webb, Dimarzio, Hancock, Lee, Bhardwaj, Brenner, Yi, Carabajal, Harding, (2011). MABEL photon-counting altimetry data for ICESat-2 simulations. AGU Fall Meeting Abstracts 1, p. 0462.
- Collin, A., Long, B., Archambault, P. (2010). Salt-marsh characterization, zonation assessment and mapping through a dual-wavelength LiDAR. *Remote Sensing of Environment*, 114 (3), pp. 520-530, doi:10.1016/j.rse.2009.10.011.
- Degnan, J. (2001). Unified Approach to Photon-Counting Microlaser Rangers, Transponders, and Altimeters. *Survey in Geophysics*, 22 (5-6), pp. 431-447.
- Douglas, E. S., Martel, J., Zhan Li, Howe, G., Hewawasam, K., Marshall, R. A., Schaaf, C. L., Cook, T. A., Newnham, G. J., Strahler, A., Chakrabarti, S. (2014). *Geoscience and Remote Sensing Letters*, 12 (4), pp. 776-780, doi: 10.1109/LGRS.2014.2361812.
- Fritsch, D., Kilian, J. (1994). Filtering and Calibration of Laser Scanner Measurements. *International Archives Photogrammetry and Remote Sensing XXX*, 3/1, 227-234.
- Fritsch, D., Cramer, M. (2013). The Relevance of RPAS for National Mapping and Cadastre Agencies in Europe. In: Blyenburgh (Ed.): *RPAS Remotely Piloted Aircraft Systems – The Global Perspective 2013/2014*, 115-118.
- Glira, P., Pfeifer, N., Briese, C., Ressler, C. (2015a). A Correspondence Framework for ALS Strip Adjustments based on Variants of the ICP Algorithm. *PFGE, Photogrammetrie, Fernerkundung, Geoinformation*, 2015(4), to appear.
- Glira, P., Pfeifer, N., Briese, C., Ressler, C. (2015b). Rigorous Strip Adjustment of Airborne Laserscanning Data Based on the ICP Algorithm. In: *ISPRS Annals of the Photogrammetry, Remote Sensing and Spatial Information Sciences* (submitted).
- Guenther, G. C., Cunningham, A. G., Laroque, P. E., Reid, D. J. (2000). Meeting the accuracy challenge in airborne Lidar bathymetry. *Proceedings of the 20th EARSeL Symposium: Workshop on Lidar Remote Sensing of Land and Sea*, Dresden, Germany.
- Heckmann, T., Hilger, L., Vehling, L., Becht, M. (2015). Integrating field measurements, a geomorphological map and stochastic modelling to estimate the spatially distributed rockfall sediment budget of the Upper Kaunertal, Austrian Central Alps. *Geomorphology*, to appear.
- Hernández-Marín, S., Wallace, A., Gibson, G. (2007). Bayesian Analysis of Lidar Signals with Multiple Returns. *Transactions on Pattern Analysis and Machine Intelligence*, 29 (12), pp. 2170-2180.
- Höfle, B., Vetter, M., Pfeifer, N., Mandlbürger, G., Stötter J. (2009). Water surface mapping from airborne laser scanning using signal intensity and elevation data. *Earth Surface Processes and Landforms*, 34 (12), pp. 1635-1649.
- Jelalian, A. (1992): *Laser Radar Systems*. Artech House.
- Kilian, J., Fritsch, D. (1993). Absolute Orientation on Photo Pairs using GPS and Laser Profiles. In: *Integrating Photogrammetric Techniques with Scene Analysis and Machine Vision*, E. B. Barret, D. M. McKeown Jr. (Eds.), SPIE Vol. 1944, Orlando, pp. 120-126.

- Korzeniowska, K., Pfeifer, N., Mandlbürger, G., Lugmayr, A. (2014): Experimental evaluation of ALS point cloud ground extraction tools over different terrain slope and land-cover types. *International Journal of Remote Sensing*, 35 (13).
- Kukko, A., Kaartinen, H., Hyyppä, J., Chen, Y. (2012). Multiplatform Mobile Laser Scanning: Usability and Performance. *Remote Sensing*, 12 (9), pp. 11712-11733; doi:10.3390/s120911712.
- Kraus, K., Pfeifer, N. (1998). Determination of terrain models in wooded areas with airborne laser scanner data. *ISPRS Journal of Photogrammetry and Remote Sensing*, 53 (4), pp. 193-203.
- Kuhn, M. (1985). Bidirectional Reflectance of polar and alpine snow. *Annals of Glaciology*, 6, pp. 164-167.
- Lefsky, M. A., Harding, D. J., Keller, M., Cohen, W. B., Carabajal, C. C., Del Bom Espirito-Santo, F., Hunter, M. O., de Oliveira Jr., R., (2005). Estimates of forest canopy height and aboveground biomass using ICESat. *Geophysical Research Letters*, 32 (22).
- Lindberg, E., Eysn, L., Hollaus, M., Holmgren, J., Pfeifer, N. (2014). Delineation of Tree Crowns and Tree Species Classification From Full-Waveform Airborne Laser Scanning Data Using 3-D Ellipsoidal Clustering. *Selected Topics in Applied Earth Observations and Remote Sensing*, 7 (7), pp. 3174-3181, doi : 10.1109/JSTARS.2014.2331276.
- Mandlbürger, G., Hauer, C., Wieser, M., Pfeifer, N. (2015a). Topo-Bathymetric LiDAR for Monitoring River Morphodynamics and Instream Habitats – A case study at the River Pielach. *Remote Sensing*, 7 (5), 6160-6195; doi:10.3390/rs70506160.
- Mandlbürger, G., Glira, P., Pfeifer, N. (2015b). Ultra high resolution point clouds from UAS-borne LiDAR for mapping complex terrain and vegetation structure. *GIM International 2015* (7), to appear.
- Markelin, L., Honkavaara, E., Peltoniemi, J., Ahokas, E., Kuittinen, R., Hyyppä, J., Suomalainen, J., Kukko, A. (2008). *Photogrammetric Engineering & Remote Sensing*, 74 (12), pp. 1487-1500.
- Measures, R. M. (1992). *Laser Remote Sensing: Fundamentals and Applications*. Krieger Publishing Company.
- Mücke, W., Deák, B., Schroiff, A., Hollaus, M., and Pfeifer, N. (2013). Detection of fallen trees in forested areas using small footprint airborne laser scanning data. *Canadian Journal of Remote Sensing* 39 (s1), pp. 32-40, doi: 10.5589/m13-013.
- Pfeifer, N., Höfle, B., Briese, C., Rutzinger, M., Haring, A. (2008). Analysis of Backscattered Energy in Terrestrial Laser Scanning Data.
- Pfennigbauer, M., Riegl, U., Rieger P., Amon, P. (2014). UAS based laser scanning for forest inventory and precision farming. Proceedings of the International Workshop on Remote Sensing and GIS for Monitoring of Habitat Quality, Vienna, Austria. <http://http://rsgis4hq.geo.tuwien.ac.at/proceedings/>.

- Puttonen, E., Suomalainen, J., Hakala, T., Räikkönen, E., Kaartinen, H., Kaasalainen, S., Liteky, P. (2014). Tree species classification from fused active hyperspectral reflectance and LIDAR measurements. *Forest Ecology and Management*, 260 (10), pp. 1843-1852, doi:10.1016/j.foreco.2010.08.031.
- Riegl, J., Bernhard, M. (1974). Empfangsleistung in Abhängigkeit von der Zielentfernung bei optischen Kurzstrecken-Radargeräten. *Applied Optics*, 13 (4).
- Rutzinger, M., Höfle, B., Hollaus, M., Pfeifer, N. (2008). Object-Based Point Cloud Analysis of Full-Waveform Airborne Laser Scanning Data for Urban Vegetation Classification. *Sensors*, 8 (8), pp. 4505-4528; doi:10.3390/s8084505.
- Sithole, G., Vosselman, G. (2004). Experimental comparison of filter algorithms for bare-Earth extraction from airborne laser scanning point clouds. *ISPRS Journal of Photogrammetry and Remote Sensing*, 59 (1), pp. 85-101.
- Swain, P., Davis, S. (1979). *Remote Sensing, The Quantitative Approach*. Swain, David (Eds.). McGraw Hill.
- Vauhkonen, J., Hakala, T., Suomalainen, J., Kaasalainen, S., Nevalainen, O., Vastaranta, M., Holopainen, M., Hyypä, J. (2013). Classification of Spruce and Pine Trees Using Active Hyperspectral LiDAR. *Geoscience and Remote Sensing Letters*, 10 (5), pp. 1138-1141, doi:10.1109/LGRS.2012.2232278.
- Wagner, W., Ullrich, A., Briese, C. (2003): Der Laserstrahl und seine Interaktion mit der Erdoberfläche. *Österreichische Zeitschrift für Vermessung und Geoinformation*, 91 (4), pp. 223-234.
- Wagner, W., Ullrich, A., Ducic, V., Melzer, T., Studnicka, N. (2006). Gaussian decomposition and calibration of a novel small-footprint full-waveform digitising airborne laser scanner. *ISPRS Journal of Photogrammetry and Remote Sensing*, 60 (2), pp. 100-112.
- Weitkamp, C. (2005). *LIDAR: Range-Resolved Optical Remote Sensing of the Atmosphere*. Weitkamp (Ed.). Springer.
- Zappa, F., Tisa, S., Tosi, A., Cova, S. (2007). Principles and features of single-photon avalanche diode arrays. *Sensors and Actuators A: Physical*, 140 (1), pp. 103-112.
- Zlinszky, A., Schroiff, A., Kania, A., Deál, B., Mücke, W., Vari, A., Székely, B., Pfeifer, N. (2014). Categorizing Grassland Vegetation with Full-Waveform Airborne Laser Scanning: A Feasibility Study for Detecting Natura 2000 Habitat Types. *Remote Sensing*, 6 (9), pp. 8056-8087, doi:10.3390/rs6098056.